Journal of Colloid and Interface Science 420 (2014) 182–188

Contents lists available at ScienceDirect

Journal of Colloid and Interface Science

www.elsevier.com/locate/jcis

Nanoscale surface characterization of biphasic calcium phosphate, with comparisons to calcium hydroxyapatite and β-tricalcium phosphate bioceramics

Rodrigo França [a,b,*], Taraneh Djavanbakht Samani [a], Ghislaine Bayade [a], L'Hocine Yahia [a], Edward Sacher [a,c]

[a] Laboratoire d'Innovation et d'Analyse de Bioperformance, École Polytechnique de Montréal, C.P. 6079, Succursale Centre-ville, Montréal, Québec H3C 3A7, Canada
[b] Dental Biomaterials Research Laboratory, Department of Restorative Dentistry, Faculty of Dentistry, University of Manitoba, 780 Bannatyne Avenue, Winnipeg, Manitoba R3E 0W2, Canada
[c] Regroupement Québecois de Matériaux de Pointe, Département de Génie Physique, École Polytechnique de Montréal, C.P. 6079, Succursale Centre-ville, Montréal, Québec H3C 3A7, Canada

ARTICLE INFO

Article history:
Received 3 October 2013
Accepted 21 December 2013
Available online 16 January 2014

Keywords:
Bioceramic
Biphasic calcium phosphate
FTIR
Hydroxyapatite
β-tricalcium phosphate
Porosity
SEM
TOF-SIMS
XPS
XRD

ABSTRACT

Objectives: It is our aim to understand the mechanisms that make calcium phosphates, such as bioactive calcium hydroxyapatite (HA), and biphasic calcium (BCP) and β-tricalcium (β-TCP) phosphates, desirable for a variety of biological applications, such as the filling of bone defects.
Methods: Here, we have characterized these materials by X-ray photoelectron spectroscopy (XPS), X-ray diffraction (XRD), scanning electron microscopy (SEM), Fourier-transform infrared (FTIR), time-of-flight secondary ion mass spectroscopy (TOF-SIMS) and laser granulometry.
Results: SEM shows clearly that BCP is a matrix made of macro-organized microstructure, giving insight to the specially chosen composition of the BCP that offers both an adequate scaffold and good porosity for further bone growth. As revealed by laser granulometry, the particles exhibit a homogeneous size distribution, centered at a value somewhat larger than the expected 500 μm. XPS has revealed the presence of adventitious carbon at all sample surfaces, and has shown that Ca/P and O/Ca ratios in the outer layers of all the samples differ significantly from those expected. A peak-by-peak XPS comparison for all samples has revealed that TCP and BCP are distinct from one another in the relative intensities of their oxygen peaks. The PO_3^-/PO_2^- and CaOH+/Ca+ TOF-SIMS intensity ratios were used to distinguish among the samples, and to demonstrate that the OH- fragment, present in all the samples, is not formed during fragmentation but exists at the sample surface, probably as a contaminant.
Conclusions: This study provides substantial insight into the nanoscale surface properties of BCP, HA and β-TCP. Further research is required to help identify the effect of surfaces of these bioceramics with proteins and several biological fluids.
Clinical relevance: The biological performance of implanted synthetic graft bone biomaterials is strongly influenced by their nanosurface characteristics, the structures and properties of the outer layer of the biomaterial.

1. Introduction

In the process of bone regeneration by synthetic grafting, the bioceramics most widely used as filling materials are hydroxyapatite (HA, $Ca_{10}(PO_4)_6(OH)_2$), β-tricalcium phosphate (β-TPC, $Ca_3(PO_4)_2$), and biphasic calcium phosphate (BCP, a mixture of HA and β-TCP), [1–3] due to their properties of biocompatibility, biodegradability, bioresorption and osteoconduction [4–6]. Each bioceramic, however, differs in its ability to participate with the dynamic physiological environment and to achieve a degree of chemical equilibrium with the host tissue, without fibrous capsule formation [7].

HA is the main component of the rigidity of vital tissues, such as bone, and has an ability to drive the further growth of bone at its surface [8,9]. Thus, the identification and distinction of different phases of bioceramic are crucial for understanding their biological effect [10–14].

The mechanical behaviors of bioactive ceramics are well enough known, and their physicochemical surface properties may now be understood in terms of their structure [15]. Both HA and β-TCP are biocompatible, nontoxic, resorbable, non-inflammatory, cause

* Corresponding author at: Dental Biomaterials Research Laboratory, Department of Restorative Dentistry, Faculty of Dentistry, University of Manitoba, 780 Bannatyne Avenue, Winnipeg, Manitoba R3E 0W2, Canada. Fax: +1 2047893916.
E-mail address: rodrigo_franca@umanitoba.ca (R. França).

0021-9797/$ - see front matter © 2013 Elsevier Inc. All rights reserved.
http://dx.doi.org/10.1016/j.jcis.2013.12.055

neither immune nor irritating responses, and have excellent osteoconductive abilities [16,17]. They differ in composition and degradation rates: β-TCP shows good ability to biodegrade and to bioresorb up to 10–20 times faster than HA, but in an unpredictable manner, so it may not provide a solid scaffolding for new bone formation [18,19]. In fact, according to Wiltfang et al. [18], the accelerated initial ceramolysis of ß-TCP ceramics did not hinder the bone-healing process, which follows the principles of a primary angiogenic reossification; in the early days, chemical impurities present in the TCP ceramics led to varying degradation times.

Biphasic calcium phosphate (BCP) is composed of a controlled mixture of HA and β-TCP [20]. According to the manufacturer's description, it is a fully synthetic bioactive, osteoconductive bone substitute, available in powder form and is already used clinically [21]. This biphasic calcium phosphate ceramic, composed of 60% HA and 40% TCP, has a chemical composition close to that of bone. It is able to gradually degrade, leaving room for natural bone [22]. The results of its implantation indicate good biocompatibility and bioresorbability, when firmly packed into the bone [23,24].

Solubility appears to be the characteristic of primary importance in the remineralization process; results showed that β-TCP has the highest solubility, followed by BCP, then HA [17,25]. In addition, the biodegradation rate increases with increasing specific surface area (powders > porous solid > dense solid), and with decreasing crystallinity and grain size [1]; this includes contaminant chemical substituents, such as F in HA or Mg in β-TCP [26]. In biphasic calcium phosphate, the limiting factor is the HA:β-TCP ratio [27].

Bone colonizes bioceramics more easily when their surfaces contain both micro- and macropores [3,4,28]. Porosity also influences biological material behavior, and is an essential parameter for a satisfactory clinical outcome [7,29,30]. For good tissue development, the pore size and interconnectivity affect fluids, nutrients and oxygen diffusion and protein adsorption, as well as cell migration and their attachment, differentiation and proliferation [20,31]. The presence of macropores (diameter >100 μm) gives the bioceramic its osteoconductive properties, and promotes cell colonization by providing a scaffold for blood vessel proliferation [32,33]. The presence of micropores (diameter <100 μm) increases the exchange surface area required for fluid penetration into tissues, and promotes the adhesion of macromolecules and proteins for selective adsorption; this presents a more suitable geometry for improved cell anchoring and cellular differentiation [15,34]. It is for this reason that the synthesis process of bioceramics is crucial.

The objective of this article is to identify and distinguish the nanoscale physicochemical features of different phases of three bioceramics, HA, β-TPC and BCP (Straumann BoneCeramic®, 60% HA–40% β-TCP), to better understanding their biological effects and to clarify the success of their use in implantation.

2. Materials and methods

2.1. Samples tested

Experiments were performed on microparticles that provide a greater exchange surface with surrounding fluids and lead to a more rapid bioceramic dissolution and, consequently, to a rapid change in the local stimulated fluid composition. The three synthetic bone substitutes analyzed were differed in their Ca:P ratios.

Hydroxyapatite (HA: $[Ca_{10}(PO_4)_6(OH)_2]$, Ca/P ratio: 1.67) was obtained from Sigma–Aldrich Inc.; β-tricalcium phosphate (β-TCP: $[Ca_3(PO_4)_2]$, Ca/P ratio: 1.5) was obtained from GFS Chemicals, and BCP (Straumann BoneCeramic 500®, 60% HA–40% β-TCP, Ca/P ratio: 1.61) was furnished by Straumann, Inc.

2.2. Protocol

All the samples were initially characterized as dry powders, referred to as the initial state. Particle dimensions were determined by laser granulometry. The surface states of the tested materials were then chemically characterized by X-ray photoelectron spectroscopy (XPS), time-of-flight second ion mass spectrometry (TOF-SIMS) and Fourier transformed infrared spectroscopy (FTIR); their crystallinities and crystal sizes were characterized by X-ray diffraction (XRD), and their morphologies by scanning electron microscopy (SEM).

2.3. Sample characterization

a. Particle size by laser granulometry:

A Coulter LS Particle Size Analyzer was used to determine the particle size distributions: the samples were dispersed in water and sonicated, as instructed by the instrument manual. The instrument provides graphical outputs of the volume, number and surface areal percentages of the particles, over a spherical equivalent diameter size range of 0.4–2000 μm.

b. Surface chemical composition by XPS:

The XPS analyses were performed using a VG ESCALAB 3 MK II; Al Kα radiation ($h\nu$ = 1486.6 eV, with an instrument resolution of 0.85 eV) was used, at a pressure below 1×10^{-9} torr. Powders were pressed into a 1×2 cm sample holders. The elements detected were observed using both survey and high-resolution, spectra, with element-dependent probe depths of ~4–5 nm. The XPS binding energy (BE) values were charge-corrected to that of uncharged adventitious carbon at 285.0 eV. This analysis method gives the energy distribution of electrons emitted as a result of the interaction between the biomaterial and incident X-rays. Their analysis gives qualitative (elements present) and quantitative (the relative concentration of each spectral peak component) information. This information permits us to evaluate the Ca:P and O:Ca ratios at the sample surfaces.

c. Crystal structure and size by XRD:

XRD was used to determine crystallinity of the samples, using a fixed incident beam angle of 5° and a detector angle range of $5° < 2\theta < 80°$. The X-ray diffractometer (PANalytic X'Pert MPD) used Cu Kα (1.54184 Å) radiation at a voltage of 50 kV, a current of 40 mA, a step size of 0.02° and a scan rate of 1.2°/min. The diffraction patterns were processed using the X'Pert High Score software. This method permits distinguishing products with the same gross chemical composition but different crystal structures (e.g., different crystal structures of calcium phosphate). Further, it permits the determination of nanocrystal size through the use of the Scherrer formula on an appropriate diffraction peak.

d. Microstructure and topography by SEM:

A JEOL JSM-7600TFE scanning electron microscope was used to image the surface structure and topography. Accelerating voltages for HA and β-TCP, using the LEI detector, were 1 and 2 kV, respectively; for BCP, using the Compo detector for the 1 μm scale and the LEI detector for the 100 μm scale, the accelerating voltages were 5 kV and 2 kV, respectively.

e. Bulk composition by FTIR:

Infrared spectra were obtained at a resolution of 4 cm^{-1}, using an M-TEC M300 photoacoustic cell mounted on a Digilab FTS700

FTIR spectrometer; 128 scans were co-added to improve S/N. Those results were particularly helpful in the identification of carbonates.

f. Surface chemical composition by TOF-SIMS:

Positive and negative ion spectra obtained with our ION-TOF IV TOF-SIMS, using a 15 kV Bi^+ primary ion source, were acquired at masses up to 500 D, while maintaining the primary ion dose at less than 10^{12} ions/cm^2 to ensure static conditions. All the positive ion spectra were calibrated to the H^+, C^+, CH^+, CH_2^+, CH_3^+, $C_2H_5^+$ and $C_3H_5^+$ peaks and all the negative ion spectra were calibrated to the C^-, C_2^-, CH^-, C_2H^-, C_3^- and C_3H^- peaks before data analysis. Sample spectra were taken over an area 50 μm × 50 μm, with an emission current of 1.0 μA in bunch mode, rastered in random mode, and presented as 128 by 128 pixels.

3. Results

3.1. Particle size by laser granulometry

The particle size distribution depends on the sample synthesis and, as in the case of the BPC, may be intentionally introduced. Fig. 1 shows the particle size distribution in volume%, which is the size distribution generally given in the literature, and Table 1 displays the statistics. HA was found to have a bimodal distribution, with peaks around 40 and 500 μm, and a mean size of 275 μm. Its high mean: median ratio (2.3) is due to the spread of the dispersion: the closer the mean and median values, the most homogenous the sample distribution, as with BCP.

β-TCP appears to be a blend of several particle sizes, as shown by its multimodal distribution. It is composited of two distinct groups of particles: the first, below 400 μm and the second, above 800 μm. The first group contains particles having three well-separated diameters, <100, ~180 and ~300 μm. The second group also contains particles having several overlapping diameters, ~1000 and ~1450 μm. As with HA, β-TCP has a high standard deviation (SD) of the mean, due to the broad range of particle sizes.

BCP has a particle mean diameter around 758 μm and a relatively small SD (287 μm), which indicates a more uniform particle diameter distribution. Both mean and median lie above the average diameter indicated by the manufacturer (~500 μm), although they may have used another technique to obtain that size.

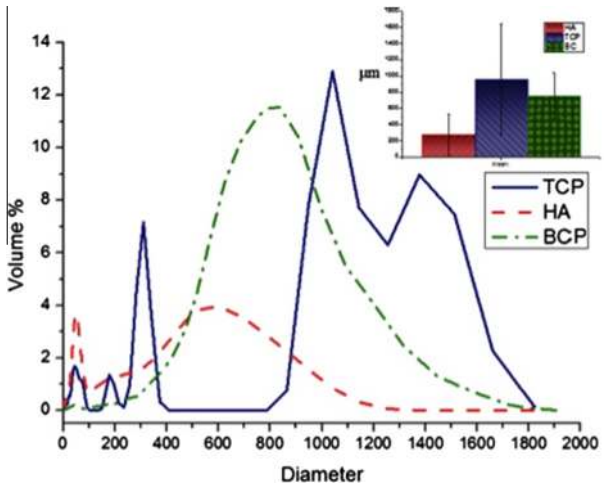

Fig. 1. Particle sizes measured by laser granulometer.

Table 1
Particle sizes determined by laser granulometry (particle volume) and XRD (crystal size) techniques.

	HA	β-TCP	BCP
Granulometry			
Mean (μm)	275	1157	758
SD (μm)	251	685	284
Median (μm)	119	845	751
Mean/median ratio	2.32	1.37	1.01
Mode (μm)	568	1080	825
XRD			
Crystal size (nm)	25	67	60
Particle/crystal ratio	11,000	17,300	12,600

3.2. Morphology by SEM

Fig. 2 shows SEM images of samples of HA (a and d), BCP (b and e) and β-TCP (c and f). Images a–c have a scale of 100 μm and indicate the macroscale morphologies of the samples, while images d–f are at a scale of 1 μm and indicate their microscale morphologies. At both of the scales, all surfaces are rough and grainy, in the order β-TCP > HA > BCP.

These pictures highlight disparate grain and pore sizes, and are clearly due to the preparation methods. Further, the presence of both micro- and macropores in the β-TCP images reflect a wide, connected pore network, having large specific area, which permits increased fluid access and better solubility.

The presence of macroporosity in both β-TCP and BCP is an essential condition for cell anchorage. While BCP appears, in the present preparation, to have no microporosity, the surface appears to be cracked and to contain some holes. These will permit minimal fluid access, as well as progressive biodegradation at grain boundaries.

3.3. Crystal lattice size by X-ray diffraction (XRD)

XRD spectra of HA and TCP samples match the JCPDS standards of these same materials, available with our instrument software. For the BCP sample, a peak-by-peak comparison, in Fig. 3, demonstrates that the powder is the expected mixture of HA and β-TCP. The ratio determined from the XRD spectrum is roughly the expected 60% HA and 40% β-TCP.

The average dimensions of the nanocrystals were determined by using the Scherrer Equation [35]:

$$t = \frac{k \cdot \lambda}{(H - s) \cdot \cos\theta}$$

where t is the crystal size (its diameter if considered spherical), λ is the wavelength of the incident wave, θ is half the 2θ value, H is the width at half peak height, and k usually takes the value 0.89. Crystal sizes were determined using the XRD peaks at $2\theta = 40°$, and are found in Table 1.

3.4. Chemical composition by high resolution XPS spectra

XPS survey spectra were used to determine the elemental compositions of the outer layers (~4.5 nm) of the samples, and are found in Fig. 4. High resolution XPS spectra were used to determine the components present in each spectrum and their relative concentrations, and are found in Fig. 5. In addition to the O1s and P2p spectra expected, C1s spectra were observed for all samples. Those spectra are due to the adsorption of hydrocarbon impurities, which does not affect the interpretation of our results. Indeed, its presence is advantageous, in that it may be used to calibrate the energy scale by setting its C–C component to 285.0 eV. The C1s

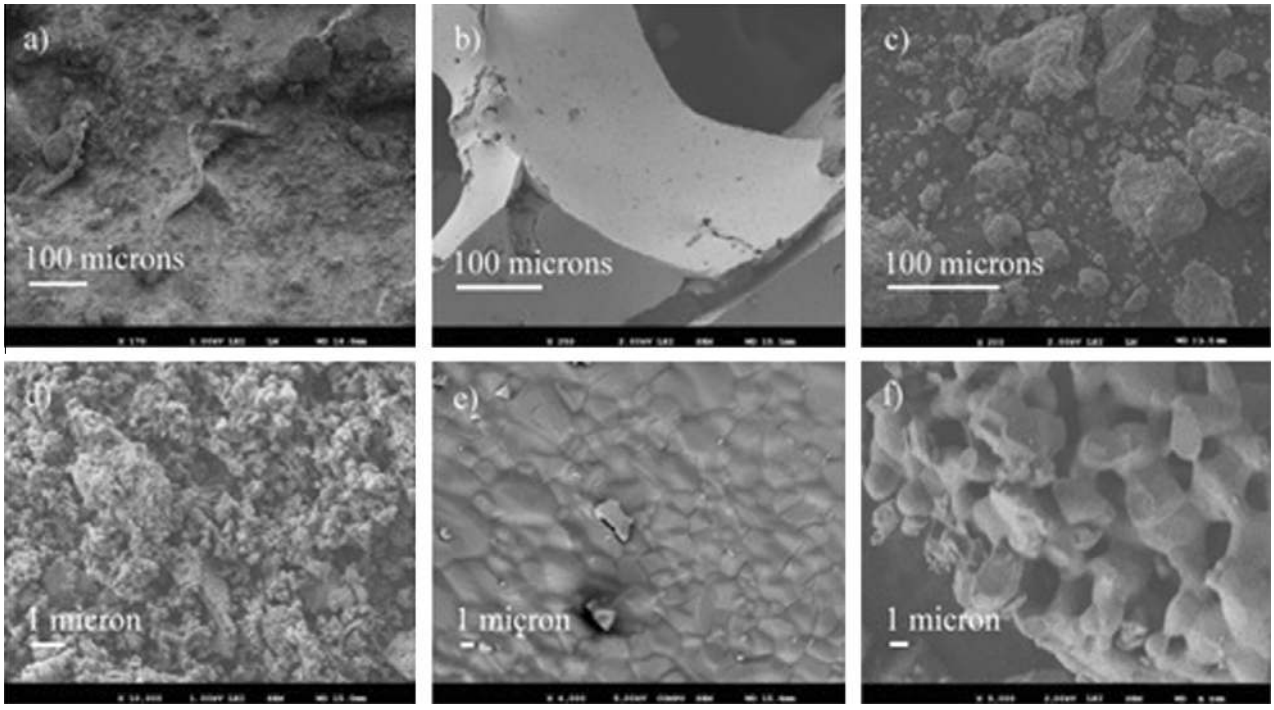

Fig. 2. SEM photomicrographs of the HA: (a) and (d), BCP: (60HA/40TCP) (b) and (e), and β-TCP: (c) and (f).

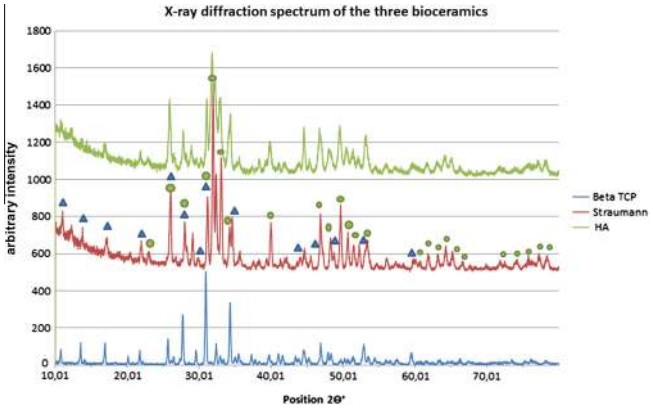

Fig. 3. X-ray diffraction (XRD) spectra of the three bioceramics.

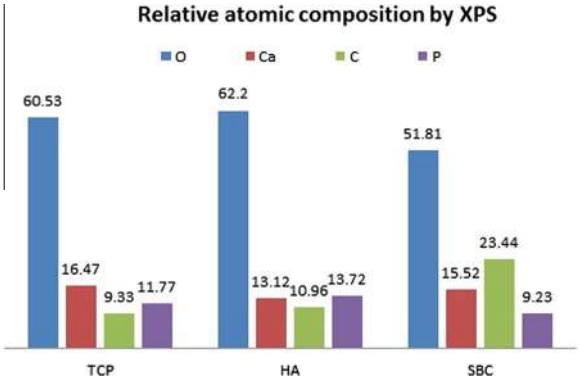

Fig. 4. XPS evaluations of the relative atomic percentages.

spectrum may also contain oxidized C, such as alcohol (~286 eV, found in all the samples), carbonyl (~287 eV, found in HA) and carbonate (~290 eV, found in β-TCP), the latter a common impurity found in calcium phosphates, due to CO_2 absorption from the air. The only other impurity found is Na, detected in the β-TCP sample at a relative concentration of 2%, and is probably due to contamination during the synthesis procedure. The relative contributions of the several carbon impurities can be quantified from the intensities of the C1s peak components.

We have compared the XPS-determined Ca/P and O/Ca ratios, features that facilitate in identifying the Ca–P phases present at the surface of the samples, as well as in determining their molar fractions. The XPS-determined atomic ratios are presented in Table 2, along with theoretical values, calculated on the basis of the chemical formulas.

While XPS probes the outer 4–5 nm of surface, which may be contaminated by reaction and/or deposition, and may not be representative of the bulk material, nonetheless, it is this outer surface that first contacts body fluids on implant, and it is indispensable to characterize it and its possible reactions.

3.5. Chemical composition by FTIR

Fig. 6 shows the infrared spectra of the three bioceramics. All samples display two strong vibrational bands, at 900–1300 cm^{-1}, from PO_4, and at 550–700 cm^{-1}, from the overlap of PO_4 and OH libration modes. In addition, HA and BCP have narrow bands at 3570 cm^{-1} from isolated OH stretching, while β-TCP and BCP display band at 1380–1580 cm^{-1}, which indicate the presence of carbonate groups. As the colored dots above the peaks in BCP indicate, it contains components of both HA and β-TCP.

3.6. Chemical composition by TOF-SIMS

Our observation of characteristic TOF-SIMS peaks was limited to the mass range of 1–100 D, for both positive and negative spectra. Fig. 7 shows positive and negative ion mode TOF-SIMS high mass resolution spectra of HA, β-TCP and BCP. Characteristic positive peaks include Ca^+, CaO^+ and $CaOH^+$; impurities, such as Na^+, and

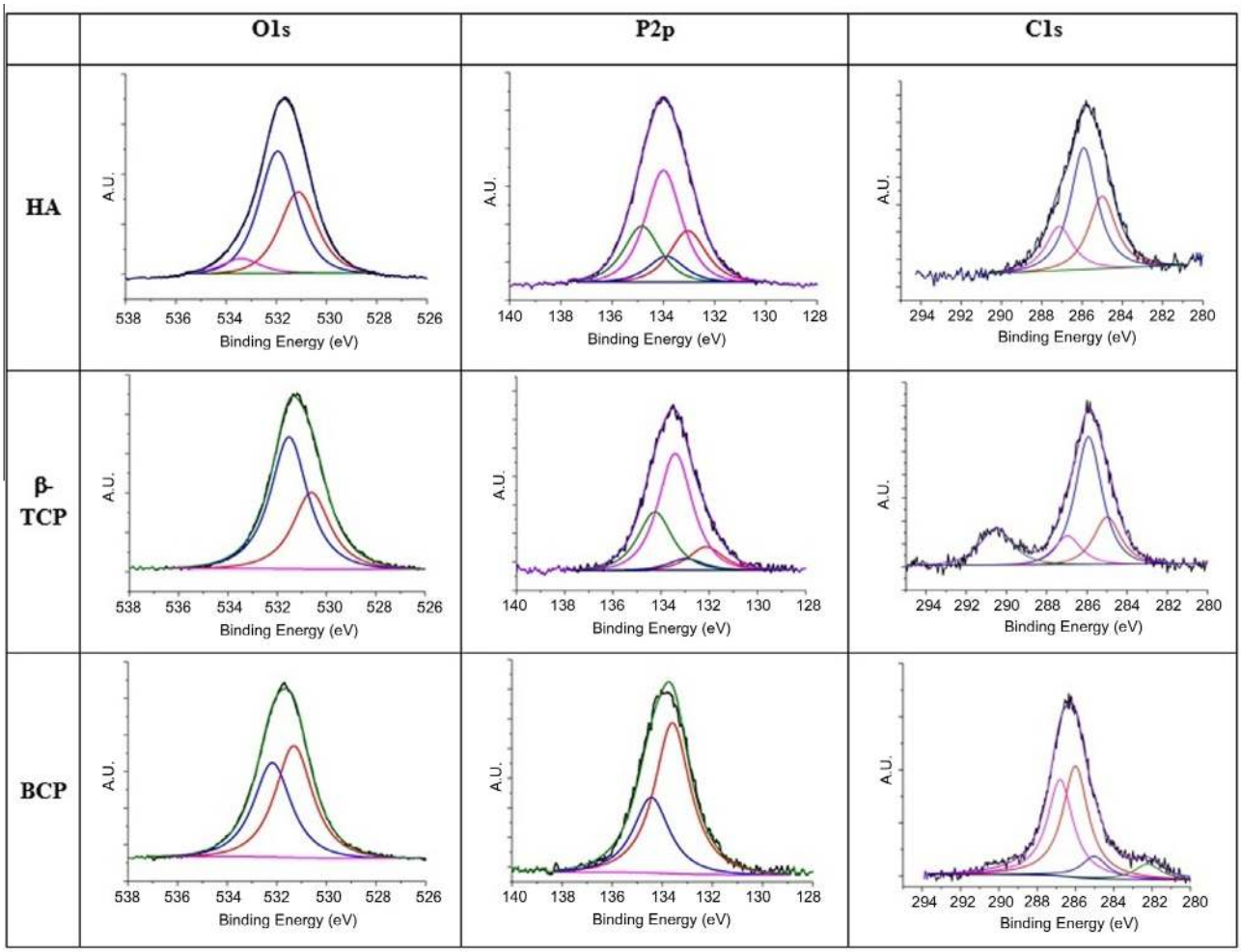

Fig. 5. XPS high-resolution results for O1s, and P2p spectra of HA, β-TCP and BCP.

Table 2
Ca/P and O/Ca atomic ratios of the three bioceramics.

	Ca/P	O/Ca	Type of results
HA	0.95	3.97	Experimental
	1.67	2.6	Theoretical
β-TCP	1.39	3.06	Experimental
	1.5	2.67	Theoretical
BCP	1.68	2.69	Experimental
	1.61	2.62	Theoretical

adventitious hydrocarbon fragments were also observed. Characteristic negative peaks include O^-, OH^-, P^-, HO_2^-, PO^-, PO_2^- and PO_3^-. The PO_3^-/PO_2^- (m/e 79/63) and $CaOH^+/Ca^+$ (57/40) intensity ratios have often been used to identify different calcium phosphates.

The intensity variations of the PO_2^- and PO_3^- peaks appear to be the most distinguishable patterns in the negative ion spectra. These peaks were present in all calcium phosphate samples, and their relative intensities changed among them [36,37]. We observed such changes in our samples. Using Bi^+ primary ions, the PO_3^-/PO_2^- ratios observed were 0.24 ± 0.01 for HA, 0.32 ± 0.01 for β-TCP and 0.35 ± 0.01 for BCP. Ratios for HA, reported by Chusuei et al. and Yan et al., were slightly higher than those for β-TCP, although Lu et al. reported that PO_3^-/PO_2^- ratios were slightly higher for β-TCP [14,36,37]. This variation may well depend on the conditions chosen for the analysis, such as the primary ion, the beam current, which may influence preferential sputtering and/or fragment ionization efficiencies [38]; if so, the PO_3^-/PO_2^- ratio may not be useful to distinguish between them.

The $CaOH^+/Ca^+$ peak intensity ratios we observed were 0.20 ± 0.01 for HA, 0.17 ± 0.01 for β-TCP and 0.10 ± 0.01 for BCP. Similar results were previously obtained by Yan et al. [37]. The presence of OH^- peaks in the negative spectra suggests that they do not originate from fragmentation reactions, but are present at the sample surface.

4. Discussion

The literature on the effect of chemical characterization is relatively sparse, compared with that on morphological characterization [39]. Previous characterizations, performed by our group, have shown that techniques such as FTIR, XRD and SEM cannot provide all the information need to distinguish the bulk composition from that of the outermost layer [40–42]. The exact composition of the nanoscale surface, and the impurities that cover it, can be probed, using tools such as XPS and TOF-SIMS.

The influence of surface impurities on bioceramic is an important topic. Contributions may often be quantified by surface characterization [10]. It is important to eliminate such impurities from bioceramics because they introduce critical defects, affecting their mechanical properties during lengthy implantation [36]. Because of this, the bioceramic synthesis process is so critical and must be so well controlled [37]. The present study demonstrates that,

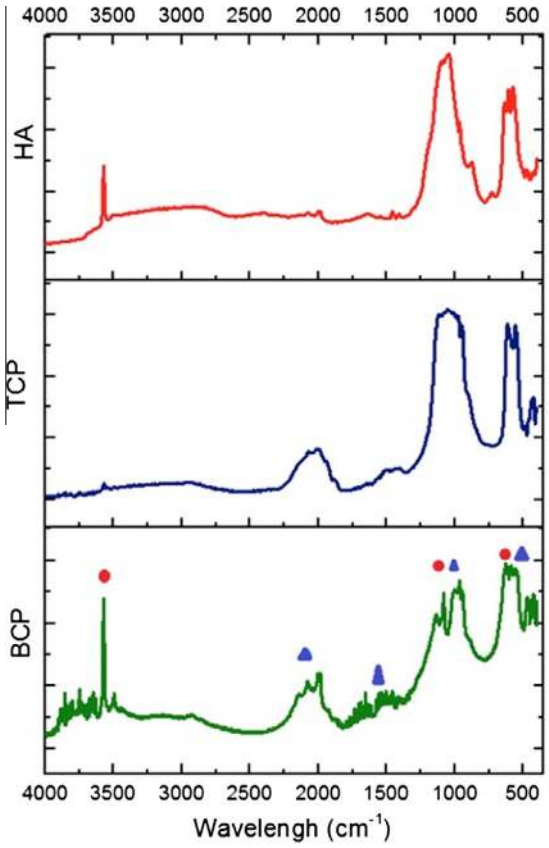

Fig. 6. Infrared spectra of HA and β-TCP and BCP.

for all the samples, the Ca/P and O/Ca atomic ratios differ significantly from those expected (Table 2). A possible reason may be the manufacturing process of the powders: ceramics are synthesized at very high temperatures (>1000 °C) and then cooled slowly, to achieve the desired phase. Further, there is always a loss of crystalline order at the outer surfaces of all nanoparticles because of a modification of atomic interactions and resultant local arrangements, leading to an amorphous surface phase. In addition, cooling is always more rapid at the surface than in the center of a particle, leaving less time for atoms to adopt a crystalline spatial arrangement. Other preparation conditions, such as the release of volatiles, the pressure and the drying conditions may affect both micro- and macroporosities. Finally, the extent of hydration may also influence the Ca/P ratios. We note that BCP seems to be the least affected by these parameters.

Table 3 contains the XPS analyses of the three samples, with the energy calibrated by setting the major component of the C1s peak to 285.0 eV. As noted earlier, this C1s component comes from adventitious hydrocarbon, and can, itself, be oxidized, depending upon its treatment. We compare our present results with those obtained on chromatography-grade samples of HA and β-TCP [36]. The component values given as O1s A, Ca $2P_{3/2}$ A and $P2p_{3/2}$ B, Table 3, are in good agreement with those given in Ref. [36]. O1s C clearly has an organic source, which is the oxidized adventitious hydrocarbon mentioned earlier.

While the source of $P2p_{3/2}$ A cannot yet be determined with confidence, it appears to indicate a species more electronegative (lower binding energy) than phosphate; correspondingly, $Ca2p_{3/2}$ B appears at a higher binding energy (a greater loss of electron density) than that bonded to phosphate, indicating its bonding to a species more electronegative than phosphate. The position of O1s B suggests that the contaminant possesses hydroxyl groups, since many metallic and semi-metallic hydroxides have O1s peaks in that energy region.

In considering the BCP data, the similarities of the XPS spectra for HA, β-TCP and BCP suggest that the O1s A and $Ca2p_{3/2}$ A components of BCP represent that material; as before, the O1s B and $Ca2p_{3/2}$ B components are associated with some other, more electronegative, contaminant. Concerning the single $P2p_{3/2}$ component for BCP, when two components are expected, the peak may be an overlap of the two expected components; that is, recalling our pre-

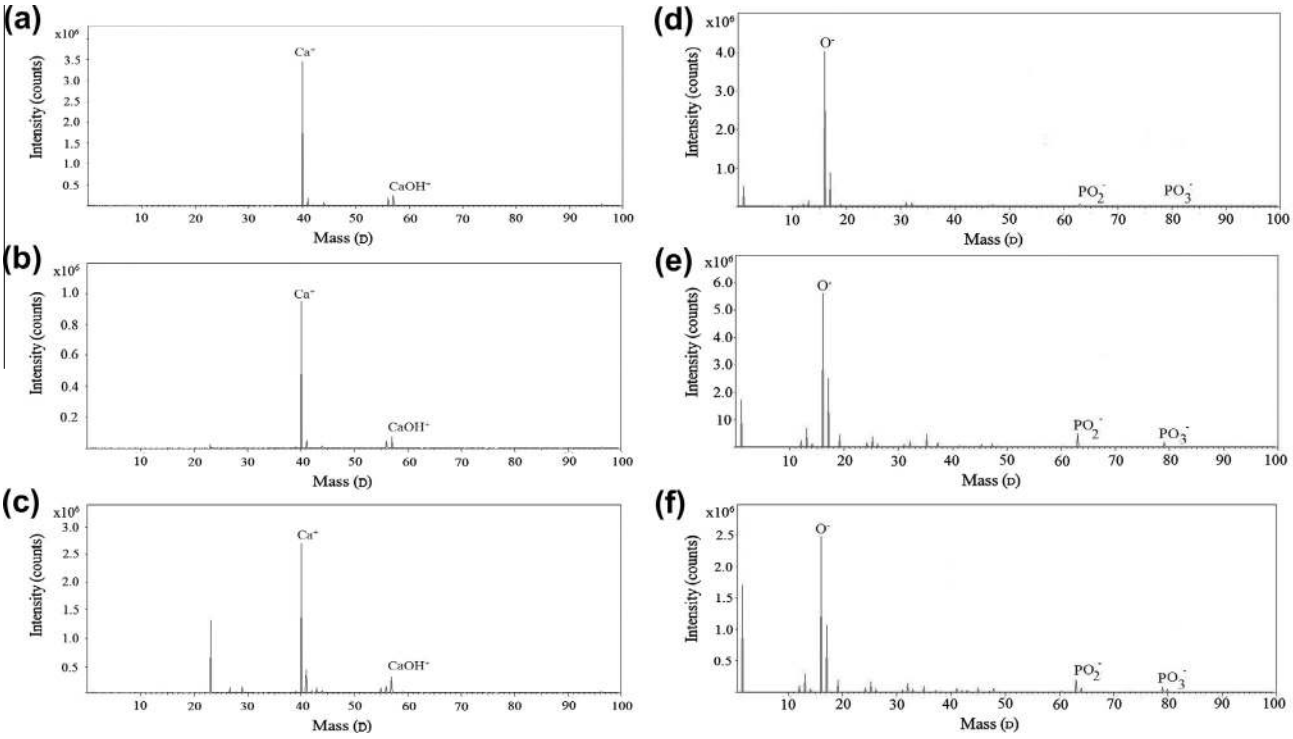

Fig. 7. Positive TOF-SIMS spectra of (a) HA, (b) β-TCP and (c) BCP; negative TOF-SIMS spectra of (d) HA, (e) β-TCP and (f) BCP.

Table 3
XPS spectral components.

	Carbon			Oxygen			Calcium		Phosphate	
	C1s A	C1s B	C1s C	O1s A	O1s B	O1s C	$Ca2p_{3/2}$ A	$Ca2p_{3/2}$ B	$P2p_{3/2}$ A	$P2p_{3/2}$ B
HA	285.0	285.9	287.1	531.1	532.0	533.4	347.2	348.1	133.1	134.0
β-TCP	285.0	285.9	290.2	530.6	531.5		347.0	347.8	132.1	133.4
BCP	285.0	285.9		531.3	532.2		347.4	348.0		133.6

viously mentioned XPS instrument resolution of 0.85 eV, an overlap of $P2p_{3/2}$ A and B for both HA (133.1 and 134.0 eV) and β-TCP (132.1 and 133.4 eV) would result in the quasi-symmetric $P2p_{3/2}$ component peak found for BCP. The $P2p_{3/2}$ component peak can, in fact be deconvoluted in this manner, although this is not a demonstration of validity.

Finally, in the process of bone regeneration, bioperformance is influenced by the following initial factors: the bioceramic dissolution rate, its chemical composition, its porosity and surface charge [1,2,15]. Continuous dissolution of the calcium-rich bioceramic may provide a saturation of calcium ions near the surface [38,43], which stimulates osteoblast-synthesized extracellular matrix and reduces osteoclastic action, which is inhibited by high local calcium concentration [27].

5. Conclusion

These results provide substantial insight into the nanoscale surface properties of biphasic bioceramic, hydroxyapatite and β-tricalcium phosphate. We measured particle diameters of these bioceramics by granulometry. XRD measurements gave crystal sizes under 70 nm for all the samples. SEM imaging revealed the presence of both micro- and macroporosity in the BCP, conditions necessary for successful incorporation. TOF-SIMS analyses revealed different intensity ratios for the PO_3^-/PO_2^- and $CaOH^+/Ca^+$ fragments, whose values may be due to the experimental conditions employed. The study also confirmed the presence of a surface layer of adventitious hydrocarbon on all the samples, which is always found on high energy surfaces. XPS measurements showed that, for all the samples, the Ca/P and O/Ca atomic ratios differ significantly from the values expected, which is due to the presence of a presently unidentified surface contaminant.

Acknowledgments

Financial support, by the ITI Foundation for the Promotion of Implantology, is gratefully acknowledged. We thank Straumann, Inc., for furnishing the Straumann BoneCeramic 500®.

References

[1] P. Ducheyne, Q. Qiu, Biomaterials 20 (1999) 2287–2303.
[2] H.-M. Kim, Solid State Mater. Sci. 7 (2003) 289–299.
[3] E. Rompen, O. Domken, M. Degidi, A.E. Farias Pontes, A. Piattelli, Clin. Oral Impl. Res. 17 (2) (2006) 55–67.
[4] X.D. Zhu, H.J. Zhang, H.S. Fan, Acta Biomater. 6 (2010) 1536–1541.
[5] C.P. Yoganand, V. Selvarajan, V. Cannillo, A. Sola, E. Roumeli, O.M. Goudouri, K.M. Paraskevopoulos, M. Rouabhia, Ceram. Int. 36 (2010) 1757–1766.
[6] S. Ni, J. Chang, L. Chou, W. Zhai, J. Biomed. Mater. Res., Part B: Appl. Biomater. 80B (2007) 174–183.
[7] H. Yuan, Z. Yang, Y. Li, X. Zhang, J.D. De Brujin, K. De Groot, J. Mater. Sci. – Mater. Med. 9 (1998) 723–726.
[8] V. Bayazit, M. Bayazit, E. Bayazit, Dig. J. Nanomater. Biostruct. 7 (2010) 267–278.
[9] J. Marchi, P. Greil, J.C. Bressiani, A. Bressiani, F. Muller, Int. J. Appl. Ceram. Technol. 6 (2009) 60–71.
[10] H.B. Lu, C.T. Campbell, D.J. Graham, B.D. Ratner, Anal. Chem. 72 (2000) 2886–2894.
[11] J.I. Langford, A.J.C. Wilson, J. Appl. Cryst. 11 (1978) 102–113.
[12] C.C. Chusuei, D.W. Goodman, Anal. Chem. 71 (1999) 149–153.
[13] D. Tadic, M. Epple, Biomaterials 25 (2004) 987–994.
[14] S. Raynaud, E. Champion, D. Bernache-Assollant, P. Thomas, Biomaterials 23 (2002) 1065–1072.
[15] X.D. Zhu, H.S. Fan, Y.M. Xiao, D.X. Li, H.J. Zhang, T. Luxbacher, X.D. Zhang, Acta Biomater. 5 (2009) 1311–1318.
[16] K. McLeod, S. Kumar, N.K. Dutta, R.St.C. Smart, N.H. Voelcker, G.I. Anderson, R.St.C. Smart, Appl. Surf. Sci. 256 (2010) 7178–7185.
[17] E. Rumpel, E. Wolf, E. Kauschke, V. Bienengräber, T. Bayerlein, T. Gedrange, P. Proff, Folia Morphol. 65 (2006) 43–48.
[18] J. Wiltfang, H.A. Merten, K.A. Schlegel, S. Schultze-Mosgau, F.R. Kloss, S. Rupprecht, P. Kessler, J. Biomed. Mater. Res., Appl. Biomater. 63 (2002) 115–121.
[19] H. Yuan, J.D. De Bruijn, Y. Li, J. Feng, Z. Yang, K. De Groot, X. Zhang, J. Mater. Sci. – Mater. Med. 12 (2001) 7–13.
[20] S.S. Jensen, A. Yeo, M. Dard, E. Hunziker, R. Schenk, D. Buser, Clin. Oral Impl. Res. 18 (2007) 752–760.
[21] L. Cordaro, D.D. Bosshardt, P. Palattella, W. Rao, G. Serino, M. Chiapasco, Clin. Oral Impl. Res. 19 (2008) 796–803.
[22] J.W.F.H. Frenken, W.F. Bouwman, N. Bravenboer, S.A. Zijderveld, E.A.J.M. Schulten, C.M. Ten Bruggenkate, Clin. Oral Impl. Res. 21 (2010) 201–208.
[23] S. Dietze, T. Bayerlein, P. Proff, A. Hoffmann, T. Gedrange, Folia Morphol. 65 (2006) 63–65.
[24] E. Kauschke, E. Rumpel, J. Fanghänel, T. Bayerlein, T. Gedrange, P. Proff, Folia Morphol. 65 (2006) 37–42.
[25] E.C. Moreno, T. Aoba, Calcif. Tissue Int. 49 (1991) 6–13.
[26] L.L. Hench, J. Am. Ceram. Soc. 74 (1991) 487–510.
[27] S. Yamada, D. Heymann, J.-M. Bouler, G. Daculsi, Biomaterials 18 (1997) 1037–1041.
[28] K. Hing, Int. J. Appl. Ceram. Technol. 2 (2005) 184–199.
[29] G. Daculsi, R. Legeros, Tricalcium phosphate/hydroxyapatite biphasic ceramic, in: T. Kokobu (Ed.), Bioceramics and their clinical applications, CRC Press, Boca Raton, FL, 2008 (chapter 17).
[30] J.C. Le Huec, T. Schaeverbeke, D. Clement, J. Faber, A. Le Rebeller, Biomaterials 16 (1995) 113–118.
[31] S. Hayakawa, K. Tsuru, A. Osaka, The microstructure of bioceramics and its analysis, in: T. Kokobu (Ed.), Bioceramics and their clinical applications, CRC Press, Boca Raton, FL, 2008 (chapter 5).
[32] P. Kasten, I. Beyen, P. Niemeyer, R. Luginbuhl, M. Bohner, W. Richter, Acta Biomater. 4 (2008) 1904–1915.
[33] C. Knabe, P. Ducheyne, Cellular response to bioactive ceramic, in: T. Kokobu (Ed.), Bioceramics and their clinical applications, CRC Press, Boca Raton, FL, 2008 (chapter 6).
[34] S. Cazalbou, D. Eichert, X. Ranz, C. Drouet, C. Combes, M.F. Harmand, C. Rey, J. Mater. Sci. – Mater. Med. 16 (2005) 405–409.
[35] P. Scherrer, Nachr. Ges. Wiss, Göttingen 26 (1918) 98–100.
[36] R.Z. Legeros, S. Lin, R. Rohanizadeh, D. Mijares, J.P. Legeros, J. Mater. Sci. – Mater. Med. 14 (2003) 201–209.
[37] A. Cuneyt Tas, F. Korkusuz, M. Timucin, N. Akkas, J. Mater. Sci. – Mater. Med. 8 (1997) 91–96.
[38] K. McLeod, S. Kumar, R.St.C. Smart, N. Dutta, N.H. Voelcker, G.I. Anderson, R. Sekel, Appl. Surf. Sci. 253 (2006) 2644–2651.
[39] K. Anselme, P. Davidson, A.M. Popa, M. Giazzon, M. Liley, L. Ploux, Acta Biomater. 6 (2010) 3824–3846.
[40] R. França, DA. Mbeh, TD. Samani, C. Le Tien, MA. Mateescu, L. Yahia, E. Sacher, J. Biomed. Mater. Res. B Appl. Biomater. 101 (8) (2013) 1444–1455.
[41] R. França, XF. Zhang, T. Veres, L. Yahia, E. Sacher, J. Colloid Interface Sci. 389 (1) (2013) 292–297.
[42] D.A. Mbeh, R. França, Y. Merhi, X.F. Zhang, T. Veres, E. Sacher, L. Yahia, J. Biomed. Mater. Res. A 100 (6) (2012) 1637–1646.
[43] R. Xin, Y. Leng, J. Chen, Q. Zhang, Biomaterials 26 (2005) 6477–6486.